ADVANCED FUNCTIONAL MATERIALS
www.afm-journal.de

Material Composition Gradient Controls the Autonomous Opening of Banksia Seed Pods in Fire-Prone Habitats

*Friedrich Reppe, Lorenzo Guiducci, Rivka Elbaum, Peter Werner, John W. C. Dunlop, David J. Merritt, Peter Fratzl, and Michaela Eder**

Plants possess intriguing mechanisms to cope with environmental stresses and disturbances, and respond to stimuli due to their sessile nature. *Banksia attenuata*, a tree or shrub species native to southwestern Australia, integrates numerous traits to persist and regenerate through reoccurring bushfires. A key trait of *Banksia* is that of serotiny: Plants can retain seeds for many years within the canopy protected inside durable seed pods (follicles), with seed release commonly triggered by the heat of bushfire, and subsequent rainfall. Here, we show that the tissue of the two follicle valves is arranged in layers, which not only counteract as a hygroscopic bi-layer, but prevent delamination as their opposed physical properties converge toward the interface. Moreover, a shape-memory effect of the active layer stores energy after the first opening step for the second opening step, ensuring delayed seed release only after the fire is extinguished. Detailed experiments reveal how structure, composition and physical properties of the tissue layers facilitate first longevity and later the complex autonomous seed release. Based on these findings, two numerical models illustrate the mechanics of the layers more deeply. These results highlight the importance of graded material properties for the function of natural actuators.

1. Introduction

Amongst the strategies plants have adopted to reproduce in fire-prone environments, serotiny, the prolonged storage of mature seeds in the plant canopy, allows populations of many Australian *Banksia* to regenerate following bushfires.[1] While many plants in temperate regions disperse their seeds from dehiscent fruits or cones when ripe,[2] mature *Banksia* seed pods (follicles) often remain closed for many years[1b] (**Figure 1**a,g), allowing plants to build large canopy-stored seed banks to repopulate after bushfires.[3] Within the two pericarp valves of each *Banksia* follicle, up to two mature seeds are retained (Figure 1b). The seeds are thus protected through extreme environmental conditions,[4] with their delayed dispersal triggered by heat and achieved by subsequent wetting and drying[3,5] (Figure 1g). As the follicle materials are not metabolically active, they operate as "pre-programmed" units driven by their complex materials architecture.[6]

The principle of serotinous seed dispersal in *Banksia* is thought to be based on the layered structure of the follicles' pericarp (Figure 1b).[6,7] The endocarp is a continuous layer of lignified sclerenchyma fibers (Figure 1c,e), in which cellulose microfibrils are closely aligned with the longitudinal axis of the fibers (Figure 1f).[6,7] In contrast, the largely thickened cell walls of mesocarp sclerenchyma (Figure 1d) show a different ultrastructure with cellulose microfibrils oriented perpendicular to the longitudinal axis of the fibers (Figure 1f).[6,7] These ultrastructural differences between the endocarp and mesocarp thus suggest that follicle opening occurs due to the actuation of a hygroscopic bi-layer, as it is known that cellulose microfibril orientations strongly control swelling and shrinking behavior.[6,7] Sclerenchyma fibers in the mesocarp are arranged

F. Reppe, L. Guiducci, P. Werner, P. Fratzl, M. Eder
Department of Biomaterials
Max Planck Institute of Colloids and Interfaces
Potsdam Science Park, 14476 Potsdam, Germany
E-mail: michaela.eder@mpikg.mpg.de

L. Guiducci
Department Speculative Transformation
Dresden University of Technology
01219 Dresden, Germany

The ORCID identification number(s) for the author(s) of this article can be found under https://doi.org/10.1002/adfm.202418592

© 2025 The Author(s). Advanced Functional Materials published by Wiley-VCH GmbH. This is an open access article under the terms of the Creative Commons Attribution License, which permits use, distribution and reproduction in any medium, provided the original work is properly cited.

DOI: 10.1002/adfm.202418592

R. Elbaum
RH Smith Institute for Plant Sciences and Genetics in Agriculture
Hebrew University of Jerusalem
Rehovot 7610001, Israel

J. W. C. Dunlop
MorphoPhysics Group, Department of the Chemistry and Physics of Materials
University of Salzburg
Salzburg A-5020, Austria

D. J. Merritt
Kings Park Science
Department of Biodiversity
Conservation and Attractions
Kings Park, Perth, WA 6005, Australia

D. J. Merritt
School of Biological Sciences
The University of Western Australia
Perth, WA 6009, Australia

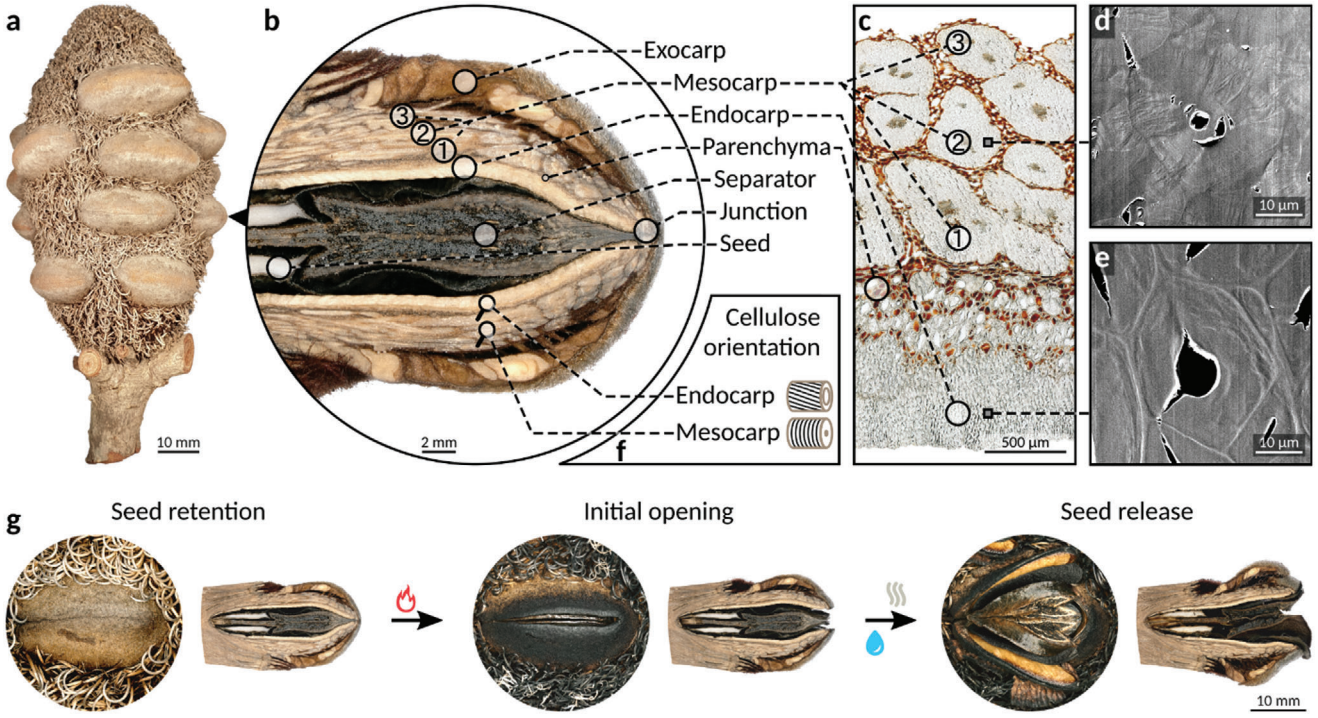


Figure 1. Structure of the *Banksia attenuata* seed pod and the opening mechanism. a) Infructescence of *B. attenuata*. b) Cut through a single follicle (longitudinal). c) Thin cross-section of mesocarp and endocarp. d) SEM-Micrograph of a mesocarp fiber (cross-section) showing the thick cell wall and the narrow lumen. e) SEM-Micrograph of an endocarp fiber (cross-section) showing a larger lumen than in the mesocarp. f) Contrary cellulose orientation in mesocarp and endocarp. g) Opening steps commencing with the mature and closed follicle retaining seeds for up to 15 years, over the initial opening within 1 minute of heat exposure, to seed release after several cycles of wetting and drying (top view on the left side and longitudinal cut through the follicle on the right side of each step).

into bundles, which are connected by tannin-rich parenchyma (Figure 1c). The mesocarp is about three times thicker than the endocarp, giving a total thickness of about 3 mm for both layers. The brittle exocarp is assumed to be mechanically irrelevant.[7]

Follicle opening in the south-west Australian species *Banksia attenuata* has been shown to be linked to the environmental conditions experienced by the individual plant.[8] In plants from northern habitats, where the weather is hotter and drier, follicles remain closed for long periods of time (up to 10 years or more) and require higher temperatures for the initial opening.[1b,7] In contrast, in plants from southern habitats, where the annual rainfall is higher, follicles are less likely to remain closed for many years, and follicle opening is initiated at lower temperatures.[1b,7] This differentiation in opening temperature results from differences in the pericarp curvature, which increases from southern to northern habitats, resulting in greater resistance to opening at elevated temperatures.[7]

The long-term stability of the follicles,[1b] the self-healing of their fragile valve junction by waxes,[9] and the two-step opening according to the local climate[1b,7] illustrate the bio-inspirational potential of the *Banksia* seed dispersal strategy. For the follicle opening event, previous studies have only explained the initial heat-triggered step via the softening of the endocarp at elevated temperatures. Hygroscopic effects were generally inferred from the cellulose orientation of the layers, but not fully resolved.[6,7]

Considering the thick and rigid pericarp, which performs an elaborate sequence of motions for seed release in response to environmental stimuli years after maturity, the characteristics presented so far can only partially explain the complex processes involved in *Banksia* follicle opening.[6,7] The present work aims to elucidate the physical properties of the follicles (mechanical characteristics, hygroscopic shrinkage, ultrastructure, chemical composition) underpinning ~~of~~ this biological phenomenon. Particular attention is paid to the hygromechanical behavior of the mesocarp, including its stress generation upon maturation, and its deformation against the resistance layer. In addition, it is explained both experimentally and by a numeric model how the follicles retain the seeds after initial opening, thereby delaying seed release until further wetting and drying events. Further modeling examines the bending principle of this thick-layered system in relation to its internal arrangement, which acts to prevent delamination (internal fracturing). To authors' knowledge, most layered floral bending mechanisms have been described by the mechanics of thin bi-layers thus far.[10] Only recently the example of pine cone scale bending has shown that such explanations may be incomplete; despite decades of study, research using more sophisticated methods has found this mechanism to be more complex than previously described.[11]

With the serotinous *Banksia* follicles, we present here an even more complex floral mechanism, which additionally incorporates the traits of durability and heat sensitivity, for plants from a fire-prone ecosystem.[12] The detailed focus of this work aims to go beyond pure insight into the persistence of *Banksia* through hostile environmental conditions, and to extend the findings of

© 2025 The Author(s). Advanced Functional Materials published by Wiley-VCH GmbH

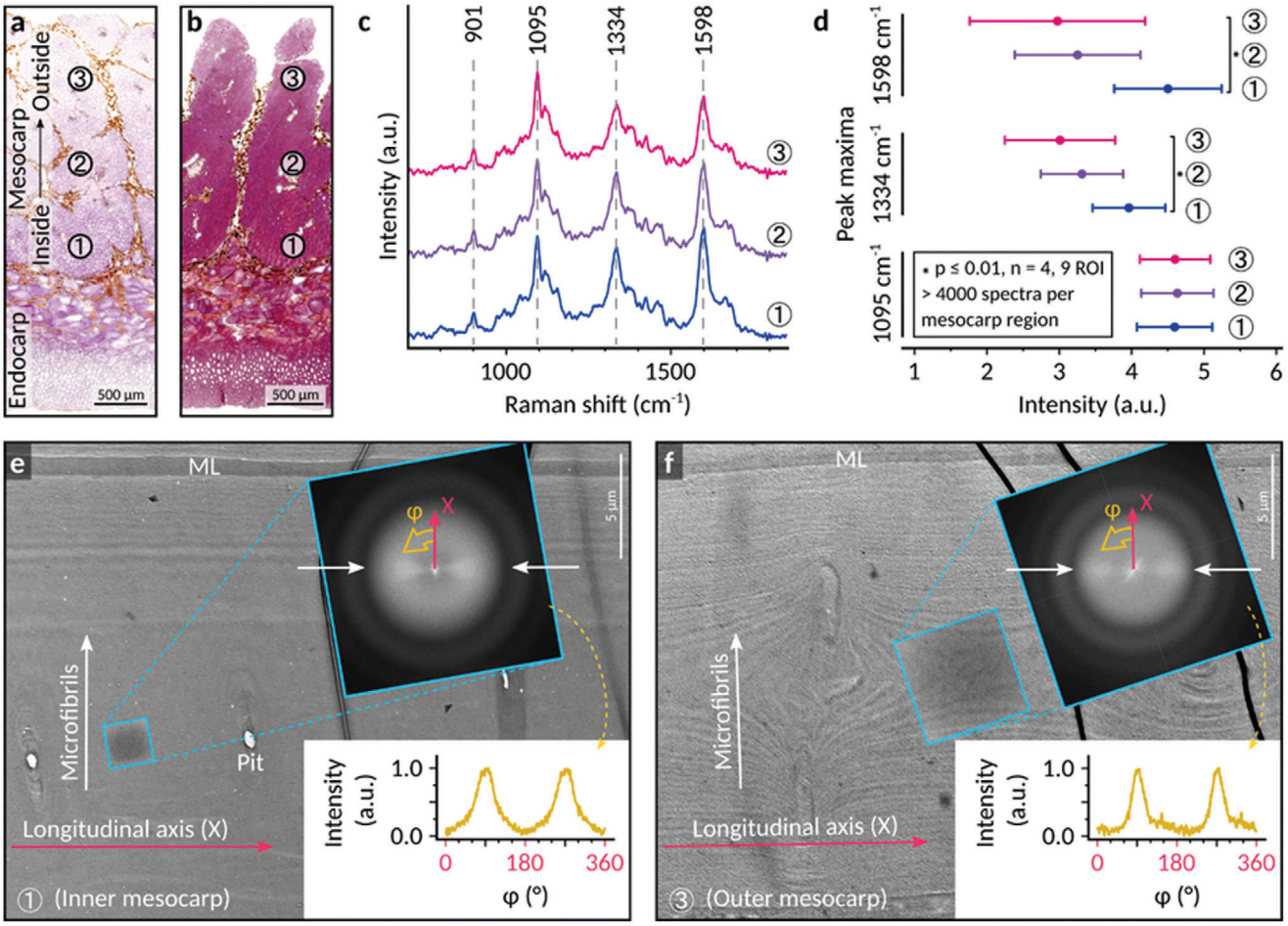


Figure 2. Lignin distribution within the *B. attenuata* mesocarp. a) Wiesner-stained cross-section. b) Mäule-stained cross-section (pink coloring indicates the presence of lignin for both stainings). c) Raman spectra of three consecutive mesocarp fiber bundles of one representative sample. d) Maximum peak intensities of four samples normalized to the maximum of the 901 cm^{-1} peak showing decreasing intensities for lignin-related peaks toward the outer mesocarp, while the cellulose-related peak at 1095 cm^{-1} remains constant. e,f) TEM-Micrographs showing the ultrastructure of a fiber from the inner mesocarp and the outer mesocarp, respectively. Diffractograms (FFT) and azimuthal intensity integrations show the cellulose orientation of a detailed image in between two pits. Data point with error bar: mean and standard deviation.

our previous studies.[4c,7,9] We demonstrate how environmental processes and the responsive behavior of the follicle material are interrelated, and develop an entirely new interpretation of a biological paradox and biomimetic challenge—the interaction of stability and motion.

2. Results and Discussion

2.1. Mesocarp Composition Shifts Gradually

In addition to providing thermal protection to the seeds, the thickness of the pericarp is necessary for the stability and longevity of the follicles. At the same time, the bending of a thick bi-layer may lead to high internal stresses, mechanical instability and delamination, which would interfere with the observed long-term seed protection and triggered follicle opening of *B. attenuata*. As a first approach, histological staining of lignin (Wiesner and Mäule) reveals compositional differences not only between active and resistance layers, but also across the thickness of the active mesocarp (**Figure** 2a,b). Both stains show gradual color shifts between the inner and outer mesocarp. The Wiesner method[13] uses phloroglucinol-HCl and strongly stains the inner mesocarp, while the outer fiber bundles show only little staining (Figure 2a). $KMnO_4$-Tris-HCl staining by the improved Mäule method[14] results in a strong coloring over the entire thickness of the mesocarp, while the outer regions appear slightly pale and the staining toward the inside of the follicle becomes more red (Figure 2b). These results suggest decreasing lignification,[13,15] due to decreasing proportions of syringyl and guaiacyl units,[14,16] and cinnamaldehyde end groups[17] toward the outside of the mesocarp. The endocarp is stained rather homogenously by both methods, indicating a consistent amount of the respective compounds as compared to the mesocarp. Only endocarp fibers close to the parenchymatic interface with the mesocarp show a slightly more intense staining.

Raman spectroscopy confirms the decreasing lignin content toward the outer mesocarp fiber bundles. The maximum intensities of the prominent peaks at Raman shifts of 1334 and

© 2025 The Author(s). Advanced Functional Materials published by Wiley-VCH GmbH

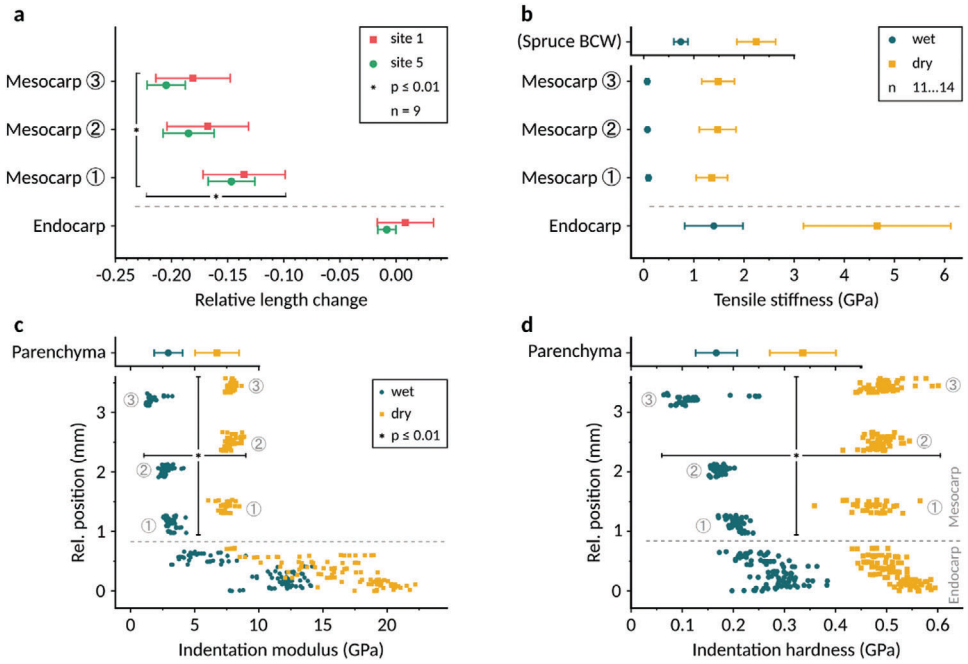


Figure 3. Physical properties of the *B. attenuata* endocarp and mesocarp. a) Shrinkage behavior, dry longitudinal tissue lengths compared to the wet state. Shrinkage is larger for less serotinous follicles (site 5) and increases significantly from the inner toward the outer mesocarp, however, with the similar tendency across the mesocarp fiber bundles for both sites (independent variables). b) Longitudinal tensile stiffness of tissue strips shows large differences between wet and dry state of endocarp and mesocarp tissue (data of spruce branch compression wood, spruce BCW, for comparison), but no differences within the mesocarp. c) Longitudinal nanoindentation modulus of wet and dry fibers and parenchyma shows converging mechanical properties between mesocarp and endocarp, with a gradual change of indentation modulus across the mesocarp, depending on the moisture state (dependent variables). d) Longitudinal nanoindentation hardness of wet and dry fibers and parenchyma with gradual hardness changes across endocarp and mesocarp similar to the indentation modulus. Numbering 1–3: consecutive mesocarp fiber bundles toward the outside of the pericarp. Data point with error bar: mean and standard deviation.

1598 cm^{-1} decrease from the inner toward the outer mesocarp (Figure 2c,d; $p \leq 0.01$, Mood's Median Test, OriginPro 2021b), where the peaks at 1598 cm^{-1} are associated with the aromatic lignin units in general[18] and 1334 cm^{-1} with syringyl lignin in particular.[19] Compared to the constant maximum intensities of the 1095 cm^{-1} peaks, which are associated with cellulose,[18a,b,20] the decrease in lignin content from inner to outer mesocarp fiber bundles could be related to an increasing proportion of the second matrix compound present in lignified plant cell walls, the more hydrophilic[21] hemicellulose. Such a compositional gradient should also be mirrored in the hygroscopic behavior of the tissue. The Raman shifts of the peak maxima remain constant across the thickness of the mesocarp, indicating a uniform molecular configuration.

Compared to compositional changes in the cell wall matrix, cellulose orientation is homogeneous across the thickness of the mesocarp, as indicated by the retardation of polarized light in the liquid crystal-based polarizing light microscope (LC-PolScope) (Figure S1, Supporting Information).[22] TEM investigations of longitudinal sections of single fibers from the inner (Figure 2e) and outer mesocarp (Figure 2f) confirm the structural uniformity. The TEM images also show a strict perpendicular orientation of the microfibrils with respect to the longitudinal fiber axis, a remarkable finding among plant fibers.[23] This is not seen so clearly in X-Ray scattering due to the presence of pits. The consistent cellulose orientation between inner and outer mesocarp fiber bundles is also in agreement with previous findings on the ultrastructural difference between the active and the resistant layer, which did not distinguish between different locations in the mesocarp (Figure 1f).[6,7] In summary, the cellulose microfibrils in the endocarp are almost longitudinally oriented compared to a perpendicular orientation in the mesocarp. This immediately suggests a potential functional significance in terms of differential swelling between the two layers[24] which will be evaluated experimentally in the following section.

2.2. Pericarp Mechanics Tuned for Serotiny

2.2.1. Graded Shrinkage of the Pericarp

Structure and composition are known to determine physical properties such as hygroscopic shrinkage of lignified fibers,[25] like those found in the pericarp of *B. attenuata*. Drying experiments show that the endocarp tissue remains dimensionally stable in the longitudinal direction (**Figure 3a**).[25a,26] In contrast, the mesocarp tissue shows remarkable shrinkage during drying (Figure 3a) and the constituent fiber bundles show a graded response. Shrinkage increases from the inner fiber bundle to the middle bundle and reaches a maximum at the outer fiber bundle ($p \leq 0.01$, Two-Way ANOVA, OriginPro 2021b). This change coincides with a decrease in hydrophobic

© 2025 The Author(s). Advanced Functional Materials published by Wiley-VCH GmbH

lignin content (Figure 2a–d), presumably in favor of hydrophilic hemicellulose.[27] Shrinkage increases similarly toward the outer mesocarp fiber bundles for both sampling sites, and there is no interaction between these independent variables ($p \leq 0.01$, Two-Way ANOVA, OriginPro 2021b). However, the overall shrinkage of all mesocarp fiber bundles is greater for less serotinous follicles—up to −0.2 of their wet length (site 5, $p \leq 0.01$, Two-Way ANOVA, OriginPro 2021b). The difference in shrinkage (longitudinal) between endocarp and mesocarp is in accordance with their cellulose orientations, as previously concluded,[6,7] while the newly discovered fine-tuning within the mesocarp suggests that a multi-layered structure is responsible for the opening process.

2.2.2. Wetting Flexibilizes Mesocarp

The endocarp and mesocarp as the resistant and active layer, respectively, can be distinguished not only by their swelling and shrinkage properties due to their characteristic cellulose orientations. Their pronounced structural differences and their moisture state also greatly influence their mechanical properties. Dry endocarp tissue strips are more than three times stiffer than wet samples in the tensile test (mean dry: 4.7 GPa, mean wet: 1.4 GPa, Figure 3b). Mesocarp tissue generally shows significantly lower stiffness values than the endocarp, due to its large microfibril angle. However, when dry, mesocarp samples are even up to 18 times stiffer than when wet (means dry between 1.3 GPa and 1.5 GPa, means wet between 70 MPa and 100 MPa).

These results may seem unusual for such a material, but they are plausible when compared with previous studies on the tensile properties of lignified fibers and theoretical considerations.[28] Not only does an increasing microfibril angle (measured from the longitudinal cell axis) decrease the stiffness, but it also influences how this stiffness changes upon wetting. Wood fibers with high microfibril angles soften more upon wetting than those with lower angles.[28] To date, no specimen with a cellulose orientation comparable to that of the *B. attenuata* mesocarp has been mechanically characterized by a tensile testing.[29] The results found here represent the properties of the lignin-hemicellulose matrix in between cellulose microfibrils. This matrix stiffness is in the same order of magnitude as that found for single wood fibers with cellulose microfibril angles ranging from about 10° to 45° at ≈3.7 GPa in the dry and 330 MPa in the wet state.[28a] Differences between the matrix stiffness values found here and those found in the literature could be related to the sample geometries.[30] Here, tissues containing lumens and possibly numerous cut cells may contribute to lower values. They could also be influenced by different ratios of hemicelluloses and lignin in the matrix. The stiffness of lignin is estimated to be 2 GPa in both dry and wet state, while the longitudinal stiffness of hemicellulose is strongly dependent on the wetting state (2 GPa dry, 20 MPa wet).[28b]

In contrast to the gradually increasing shrinkage from the inner to the outer mesocarp, and the compositional changes, no significant differences in tensile stiffness can be determined for these tissue regions. This is not surprising, especially in the dry state, since lignin and hemicellulose are known to be similarly stiff in the absence of water.[28b] However, in the wet state, the stiffness of hemicellulose decreases by 99%, while the stiffness of lignin remains unaffected.[28b]

In terms of follicle opening mechanics, these results draw a picture of a structure which is highly flexible when wet (i.e., throughout the growth and maturation phases of the follicles, and during periods of rainfall once the follicles are mature), especially the mesocarp. As it dries, the tissue stiffens, temporarily toughening up for seed protection over longer periods. In addition, the interaction of flexibility and stiffening is an essential feature for the stepwise opening of the follicle, as will be shown later.

2.2.3. Opposed Layer Properties Converge Gradually

The high spatial resolution of nanoindentation reveals mechanical differences between the mesocarp fiber bundles, but also within the endocarp layer. The indentation modulus and hardness of the mesocarp are higher in the dry state than in the wet state, with this measured difference increasing for mesocarp fiber bundles further away from the endocarp (Figure 3c, $p \leq 0.01$, Two-Way ANOVA, OriginPro 2021b). This difference is evident when comparing the means of the tissue regions in the dry and the wet state. In the inner mesocarp the dry indentation modulus is 7.45 GPa, compared to 3.12 GPa wet. A fiber bundle in the middle of the mesocarp has a modulus of 7.89 GPa (dry) versus 2.75 GPa (wet), and in the outer mesocarp, the dry modulus is still 7.80 GPa, while the value drops to 1.66 GPa in the wet state. The indentation hardness shows similar trends (Figure 3d). From the inner mesocarp, over a fiber bundle in the middle, to the outer mesocarp, the average dry hardness is 476, 486, and 494 MPa, respectively, while the same tissue regions show 206, 173, and 119 MPa in the wet state (Figure 3d). This increasing contrast in indentation properties between the dry and wet states toward the outside of the mesocarp can be related to the decreasing lignin content,[31] which leads to an increasing flexibilization of the mesocarp tissue toward the outside of the layer upon wetting.

Within the endocarp, a pronounced stiffness gradient is observed, starting with lower indentation moduli at the parenchymatic interface with the mesocarp (minimum dry: 7.50 GPa, minimum wet: 3.19 GPa) and increasing toward the edge of the layer at the inner cavity of the follicle (maximum dry: 22.20 GPa, maximum wet: 14.16 GPa). The Spearman correlation coefficients (calculated using Origin Pro 2018) between the location of the indentation and its modulus of indentation are −0.73 for the dry state and −0.62 for the wet state. The successive change in mechanical properties between active and resistant layers could be a result of both the changing lignin content[31a] (Figure 2a,b) and the slight variation in cellulose orientation as indicated by the LC-PolScope measurement[31b] (Figure S1a, Supporting Information). It is likely that these property gradients are essential for the long-term stability of the follicle. The high stiffness at the edge of the endocarp, toward the inner cavity (Figure 3c), provides resistance that ultimately allows the multilayered pericarp to bend during opening. The more flexible tissue toward the interface prevents internal fracture (delamination) and allows drying stresses to concentrate at the valves' junction. Parenchymatic tissues at the layer interface, and in between the mesocarp

© 2025 The Author(s). Advanced Functional Materials published by Wiley-VCH GmbH

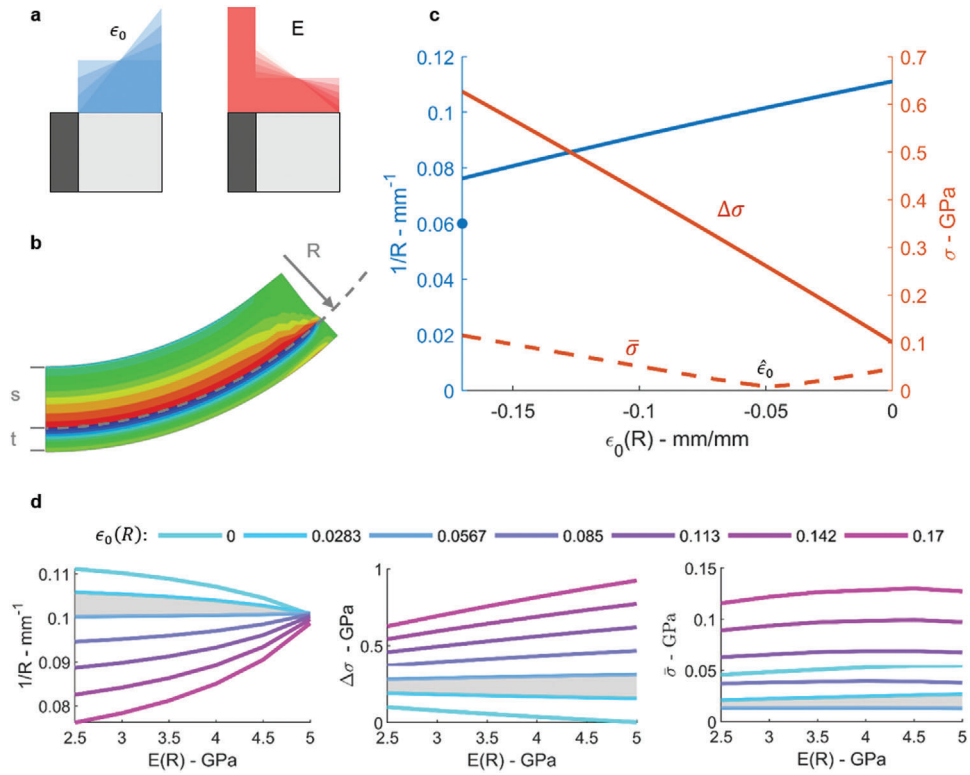


Figure 4. Finite element model of the *B. attenuata* pericarp. a) Shrinkage and Young's modulus gradients investigated in the model (dark grey: endocarp; light grey: mesocarp). b) Upon shrinkage of the mesocarp, the mesocarp bends in a circular arc with radius R at the interface of endocarp and mesocarp; colormap shows longitudinal stress across the model. c) FE data showing the curvature 1/R, differential stress $\Delta\sigma$ at the endocarp-mesocarp interface, and average longitudinal stress in the mesocarp $\bar{\sigma}$ for an increasingly steep shrinkage gradient (at uniform and constant mesocarp modulus). Shrinkage: the blue dot marks the value of curvature predicted by the Timoshenko formula for bimetal thermostats. d) Same quantities as in c) upon changes in both shrinkage and modulus gradients.

fiber bundles, are assumed to absorb stresses. These parenchyma tissues have indentation moduli similar to the mesocarp sclerenchyma, but for smaller cell wall thicknesses.

To further illustrate the functional relevance of these material-related gradients for the opening mechanism, a numerical finite element (FE) model based on the experimental data, is used. The model allows parametric testing of the effect of the property gradients (i.e., shrinkage and Young's modulus) on stress and deformation in a thick bilayer. Here, an actively shrinking mesocarp layer and a passive (non-shrinking) endocarp with a thickness ratio of 3:1 was simulated for different gradients in shrinkage and Young's modulus of the mesocarp (**Figure** 4a). The average shrinkage of the mesocarp was kept constant, meaning the gradient is determined solely by the shrinkage strain at the interface, $\in_0(R)$. The deformation is captured by the curvature $1/R$ of the modeled pericarp in the deformed state, measured at the interface of endocarp and mesocarp; the stress is shown in terms of the differential longitudinal stress $\Delta\sigma$ at the endocarp-mesocarp interface (Figure 4b), and the average longitudinal stress in the mesocarp $\bar{\sigma}$ (calculated as the spatial average of the absolute value to avoid spurious canceling of positive and negative values). While the FE model shows that the bilayer always deforms into a perfectly circular arc shape (akin to the Timoshenko thin bilayer model), the resulting curvature increases with steeper shrinkage gradients (smaller values of $\in_0(R)$), despite all shrinkage gradients possessing the same mean value within the mesocarp. Note that the thick tissue cannot be described by the Timoshenko model which assumes thin bilayers (see Figure 4c). Steeper shrinkage gradients, while keeping the Young's modulus uniform across the mesocarp, result in a lower interfacial stress $\Delta\sigma$ (Figure 4c). The lowest interfacial stress is obtained for the highest gradient $\in_0(R) = 0$, for which continuity of zero shrinkage is ensured at the mesocarp-endocarp interface. More interestingly, the average longitudinal stress in the mesocarp $\bar{\sigma}$ changes for different shrinkage gradients and instead of being monotonic, it shows a minimum for a gradient characterized by an interfacial shrinkage strain of $\hat{\in}_0$. These apparently counterintuitive observations become clearer considering the role of the bilayer finite thickness. In a thick straight bilayer of length l_0 that bends into a thick circular arc the total strain $\in$ of its longitudinal fibers will be proportional to the fibers' position across the beam thickness, such that in the deformed state $l = l_0\,(1 + \in) = r\theta$. Here, r is the radial position of a longitudinal fiber (Figure 4b), varying in $(R - s;\ R)$ for mesocarp fibers and $(R;\ R + t)$ for endocarp fibers, R being the radius at the mesocarp-endocarp interface. The curvature angle will be $\theta = l_0/(R + t/2)$ (here, for simplicity, we assume that the passive endocarp has a neutral axis at its centerline). Substituting, we

© 2025 The Author(s). Advanced Functional Materials published by Wiley-VCH GmbH

obtain $\varepsilon\ (r) = \frac{r}{l_0}\ \theta - 1 = \frac{2(r-R)-t}{2R+t}$. This equation describes a linear strain profile across the mesocarp, that starts from a finite value $\varepsilon\ (R) = -\frac{t}{2R+t}$ at the interface of endocarp and mesocarp. Obviously, taking $\in_0 (r) = \in(r)$ will minimize, and should put to zero, the longitudinal stress in a global sense, since, by construction, the total strain will match the imposed shrinkage, as $\sigma = E(\in - \in_0)$. Indeed, in the FE data we find a signature of a $\bar{\sigma}$ minimizing gradient for $\hat{\varepsilon}_0 = \varepsilon_0\ (R) = -0.05$ (see the red dashed curve in Figure 4c). However, being non-zero, $\hat{\varepsilon}_0$ causes a shrinkage discontinuity (remember that shrinkage is zero in the endocarp) and therefore a finite interfacial stress $\Delta\sigma$. Clearly, a shrinkage gradient that maximizes curvature $1/R$ while at the same time minimizing the stress in a global ($\Delta\sigma$) and local sense ($\bar{\sigma}$) is not well defined, at least for linear gradients. Our study illustrates that in a thick graded bilayer like the pericarp of the *B. attenuata* follicle, a tradeoff must be found. Higher, steeper shrinkage gradients (for $\varepsilon_0(R) > \hat{\varepsilon}_0$) will increase the overall curvature and minimize the interfacial stress—but at the expense of an increased stress in the outer mesocarp fibers. Conversely, lower, flatter shrinkage gradients (for $\varepsilon_0(R) < \hat{\varepsilon}_0$) will result in a much lower curvature and increased stress in the inner fibers close to the mesocarp-endocarp interface (see maps in Figure S2, Supporting Information for a visual comparison). The shrinkage gradient for which $\varepsilon_0\ (R) = \hat{\varepsilon}_0$ appears to be somewhat special in that it minimizes the average stress across the mesocarp at the expense of a slightly higher interfacial stress and lower curvature. Interestingly, this is supported by the relative length changes measured in excised strips of the mesocarp (Figure 3a). These considerations further reinforce our hypothesis on the functional role of shrinkage gradients as an additional element to reduce mechanical stress both at the interface and across the parenchymatic layer.

Now the basic functional role of the shrinkage gradient has been explained, we can consider the additional effect of a modulus gradient. In this case, the effect is quite straight forward. For low shrinkage gradients (pink curves in Figure 4d), an increase of the modulus gradient will produce an increase of both the curvature and the stress, whereas the opposite is true for high shrinkage gradients (cyan curves in Figure 4d). Therefore, the simultaneous maximizing of curvature and minimizing of stress by changes in the modulus gradient is not possible. Interestingly, our parametric study shows that at specific intermediate values of shrinkage gradients, both curvature and stress are independent of the actual modulus gradient present in the mesocarp (grey shaded areas in Figure 4d corresponding to substantially flat curves). In particular, the shrinkage profile $\hat{\varepsilon}_0$ discussed earlier falls exactly in this range. Such decoupling of $1/R$, $\Delta\sigma$ and $\bar{\sigma}$ from a specific modulus gradient could be beneficial (or even selected for) in the pericarp of the *B. attenuata* follicle in which the relative concentrations of lignin and hemicelluloses simultaneously affect both the shrinkage and modulus distributions across the pericarp (with large variations between dry and wet state, see chapter 2.2.2). The FE simulations are relatively simplistic in comparison to the true 3D geometry of a *Banksia* follicle. The simulations are 2D, have isotropic material properties, and use linear elastic material properties only. Despite these simplifications, such simulations allow for the testing of the relative importance of design parameters such as materials property gradients, and geometric features on the performance of biological actuators, which is otherwise not possible using a purely experimental approach.

2.2.4. Loading and Shape Memory of the Mesocarp

The outer mesocarp is particularly relevant for the follicle opening, as the dimensional and mechanical response of these "most active" fiber bundles to moisture is remarkably high (Figure 3a,c,d). Furthermore, the response of the endocarp and mesocarp is coupled, with each layer constraining its neighbor in a manner which in turn varies with moisture content. To explore the role of constraint on the mechanical response of the mesocarp, precise multi-cycle combined tensile and hydration tests were performed (Figure S3, Supporting Information, **Figure 5a**). Constrained drying of single fibers from the outer mesocarp can generate stresses of up to 40.7 MPa (mean, Figure 5a,b: steps 1–2). Intriguingly, after the removal of the stress at constant humidity (dry-state), a residual strain is observed (Figure 5a,b: step 3). This residual strain then relaxes only after further cycles of wetting and drying (Figure 5a,b: steps 4–9) at zero load (free ends). This observation is akin to shape memory behaviors seen in some metals and polymers.[32] As the experimentally measured elastic and swelling strains alone cannot account for the relaxation behavior seen, we hypothesize the presence of a load (and time) dependent "internal strain." If we do this the shape-memory behavior can be reproduced using a simple phenomenological model in which the total strain is given by the sum of elastic (ε_{el}), swelling (ε_{sw}), and internal strains (ε_{int}).

$$\varepsilon_{total} = \varepsilon_{el} + \varepsilon_{sw} + \varepsilon_{int} \tag{1}$$

We assume that the elastic strain is related to the stress through Hooke's Law, $\sigma = E\varepsilon_{el}$, where E is the Young's Modulus, and the swelling strain is given by $\varepsilon_{sw} = \alpha\ c$, where α is the coefficient of swelling and c is the moisture content (the effect of complete wetting is not included). The simplest model to describe internal strain is that it increases at a rate proportional to the current stress and relaxes at a rate which is proportional to its current value:

$$\dot{\varepsilon}_{int} = k_1\sigma - k_2\varepsilon_{int} \tag{2}$$

k_1 is assumed to be constant, and k_2 is the relaxation rate, is taken to increase with the moisture content. These equations can be solved numerically and reproduce the experimental stress relaxations observed at each change in relative humidity as well as the recovery of the internal strain upon cyclic loading at zero stress (Figure 5e,f).

This residual, or internal, strain is likely to originate from the same mechanism which causes mechanosorptive creep in lignified fibers—the molecular rearrangement between the cell wall polymers.[33] In this case, hydrogen bonds within a stretched sample break upon sorption, and reconnect at another position.[34] After unloading, not only time, but also humidity cycles, are required for the samples to partially recover their initial length.[34b] In addition, the concept of "hidden-length" may also play a role for this residual strain.[35] If the matrix consists of long chain disordered polymers (e.g., hemicelluloses), they may

© 2025 The Author(s). Advanced Functional Materials published by Wiley-VCH GmbH

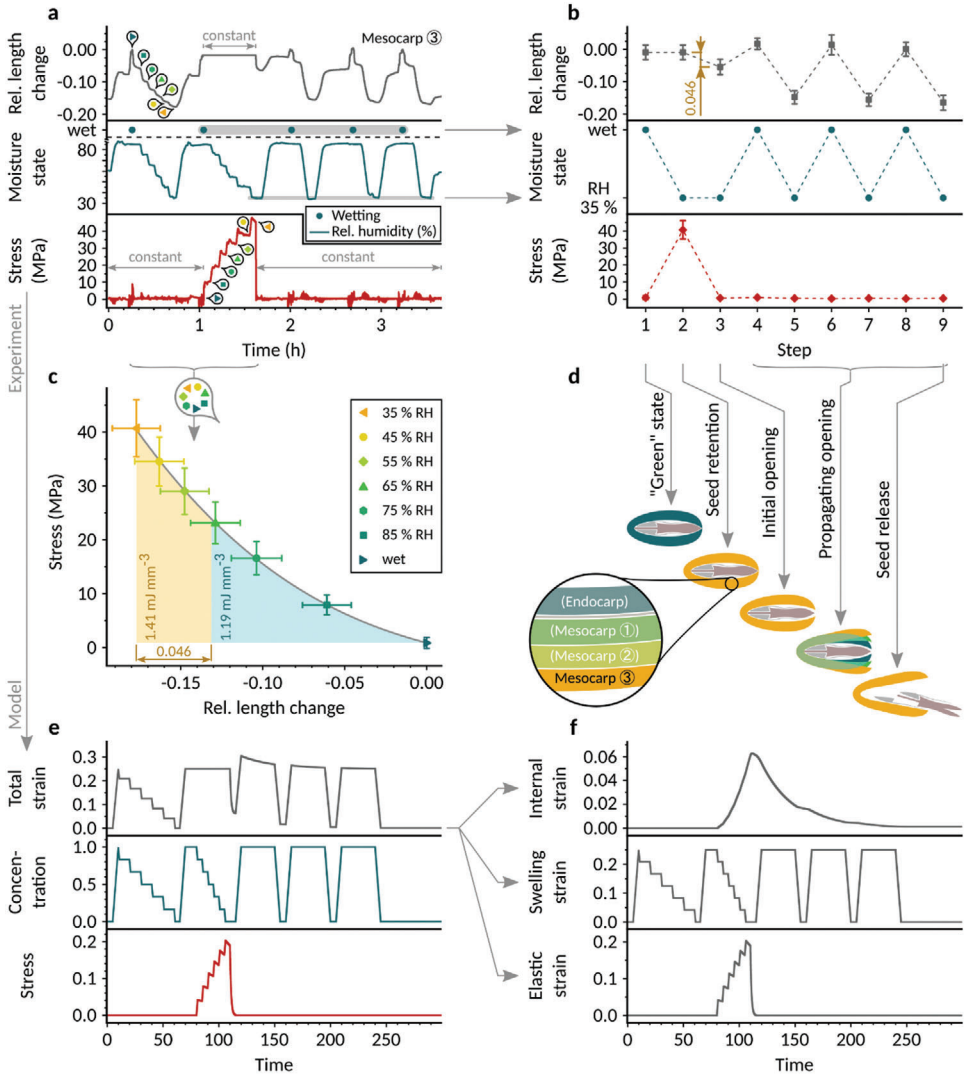


Figure 5. Shrinkage and shape memory of *B. attenuata* outer mesocarp. a) Tensile experiment of a single fiber in cyclically changing moisture conditions, simulating fiber behavior during maturation and opening of the follicle after one initial cycle. First moisture cycle at zero-load (contraction), second cycle with fixed ends showing stress development (analogous to the maturation of the follicle), stress release causing partial contraction (analogous to the initial, fire-triggered opening), and three more moisture cycles leading to shape recovery (as necessary for complete follicle opening). b) Summary of all single fiber measurements showing the extreme conditions (wet and 35% RH) of each moisture cycle with the corresponding relative length change and stress. c) Dependency between shrinkage and stress generation of single fibers from the outer mesocarp due to drying, based on the moisture steps of the first two experimental moisture cycles. Integration below the curve: energy involved in the first opening step (yellow, based on partial shrinkage (b) after impeded drying) and second opening step (blue, rest of the energy). d) Illustration of how the hygroscopic behavior of single fibers from the outer mesocarp affects the follicle opening. e) Model to reproduce the behavior of the outer mesocarp numerically. f) The different strain components parsed, which interact during stress generation, initial opening, and cycling valve deflection until seed release of *B. attenuata* follicles. Data point with error bar: mean and standard deviation (n = 8).

become mobile due to hydration and unfold upon loading. Upon drying under load, these polymers may remain extended as their mobility decreases and only relax to their initial state upon rehydration. Whether such a mechanism is involved in the observed behavior of the mesocarp is unclear. The shape memory effect itself, however, can be important for protecting the seed from damage after the first opening step.

From the experimental data, we can determine the energy density in the outer mesocarp during drying, which generates stresses when deformation is constrained and causes shrinkage when the tissue is free to contract (Figure 5c). The total energy density is 2.60 mJ mm^{-3} (integrated along a third-order polynomial fit of the data points with OriginPro 2021b). 1.41 mJ mm^{-3} can be attributed to the partial (elastic) contraction (Figure 5c), considering the limited relative deformation of −0.046 during unloading after constrained drying (Figure 5b: steps 2–3). In this case, the deformation may be limited by the loss of flexibility during drying, which stiffens the stretched tissue, compared to the wet state (Figure 3b). In terms of follicle opening, the energy portion of this elastic contraction is responsible for the first opening

© 2025 The Author(s). Advanced Functional Materials published by Wiley-VCH GmbH

step upon heat exposure. The remainder of the energy can be attributed to the second opening due to humidity cycles, which again flexibilize the tissue for further contraction to an average relative deformation of −0.166 of the wet length (Figure 5b: steps 4–9). These experimentally derived energy values are likely to be smaller than those of the follicles in situ, where the mesocarp tissue generates stresses as it dries from the green state,[36] but the data can be considered an approximation of the driving force behind the natural opening process. The fact that the relationship between stress and relative length change is not linear is due to the stiffness of the material, which changes with moisture. Interestingly, the hyperbolic function found here is similar to the relationship between load and velocity of tetanic contraction found for skeletal muscle fibers.[37] For the *Banksia* mesocarp fibers studied here, the slope of the fit gives the stiffness for each moisture level. In the wet state, the stiffness is 80 MPa—comparable to the tensile test data in Figure 3b. However, in the dry state at 35% relative humidity, the slope in Figure 5c shows a stiffness of 424 MPa, which is only about 30% of the stiffness determined by tensile tests on dry tissue strips (Figure 3b). These tensile test strips were exposed to water during sample preparation. They were allowed to dry unimpededly so that they could shrink freely. It can be speculated that more hydrogen bonds were newly formed in this case than in the case of drying with fixed ends. This could explain the difference in stiffness, depending on whether the tissue is in the process of stress generation or free shrinkage. During the final loading at 60% relative humidity after the cyclic experiment, the fibers show a stiffness of 1.3 GPa (mean, standard deviation: 0.2 GPa, n = 8, Figure S4a, Supporting Information). This value is similar to the tensile tests of tissue strips (Figure 3b). Therefore, it supports the hypothesis that the dry stiffness of the outer mesocarp is only temporarily reduced due to the impeded shrinkage and stress generation. The stresses generated when the fibers are dried from the wet state at 60% relative humidity (Figure 5c) are close to the yield point of the final loading after the cyclic experiments (Figure S4b, Supporting Information). This indicates that the material reaches its elastic limit when dried with fixed ends.

Stepwise stress generation, restrained contraction, and complete shrinkage of individual fibers from the outer mesocarp against more dimensionally stable tissue layers correspond to the macroscopic opening steps of *B. attenuata* follicles (Figure 5b,d) as they can be observed in the field. During the first drying of the follicle, the mesocarp pre-loads against the resistant endocarp[7] and against the junction of the valves, years before the rapid follicle opening upon heat triggering. These mesocarp-generated stresses are expected to gradually decrease toward the interface of mesocarp and endocarp. Analogous to the shrinkage gradient discussed earlier (Figure 3a) and the modeled longitudinal stress within the mesocarp (Figure 4), such a stress gradient could contribute to the long-term stability and counteract delamination of the interface between the active and resistant layer. The stresses within the mesocarp might increase even further during a bushfire as the tissue contracts (Figure S5, Supporting Information), and facilitate the initial opening of the follicle. During this initial opening, the increased fiber stiffness limits the possible contraction of the active layer during unloading, possibly most in the outer mesocarp (Figure 3c). As a consequence, the follicle valves deflect only partially—an essential function to retain (and thus protect) the seeds, beyond the time of the bushfire. Subsequent wetting and drying leads to progressive shrinkage of the mesocarp (compare Figure 5b: steps 4–9) against the endocarp in each drying step, with each cycle increasing valve deflection and enabling for seed release, once the fire has been extinguished.

3. Conclusion

Our detailed investigation of the *B. attenuata* pericarp tissue shows that the autonomous movement of layered plant organs can have a far more complex background than often described. The case presented here shows that active and resistant layers are not only built to counteract to generate motion, but they are also built to interact on the micro level to ensure longevity of function. Shrinkage within the follicle valves of *B. attenuata* is greatest on the outer edge of the active mesocarp and gradually decreases toward the interface with the resistant endocarp, which does not shrink longitudinally. Similarly, the flexibilizing effect of wetting is greatest where the shrinkage is greatest. Interestingly, the property gradients within the mesocarp appear to be a result of changes in lignin content, rather than cellulose orientation. The macroscopic differences in shrinking between the mesocarp and endocarp can be ascribed to differences in cellulose orientation (perpendicular versus longitudinal, respectively). It seems that fine tuning of shrinking within the mesocarp is achieved by the presence of a lignin gradient. The resistance of the endocarp increases from the interface with the mesocarp and reaches a maximum at the edge of the layer. In a numerical finite element model, we could show that these material gradients are a sound strategy to improve the actuation capacity of the pericarp. It maximizes deformation and reduces the overall stress. At the same time, the effects of drying on shrinkage and stiffness profiles are decoupled. The most active part of the mesocarp shows a shape memory effect, which we were able to parse into different strain components using a numerical model. This effect allows the active layer to retain part of the opening energy after the first follicle opening step, to protect the seeds inside the follicles throughout the heat of a bushfire that initiates this opening, and to subsequently release the seeds after rainfall. Our findings may provide new inspiration for biomimetic approaches, which often focus on high aspect ratios of layer dimensions and a rather narrow range of property-function relationships.[38] As actuating layers become thicker, more complex stress states come into play, which can limit their use and require more detailed compositional, structural, and mechanical modulation—as has been observed in *Banksia* follicles. Potentially these approaches may then open up a whole new perspective for autonomous materials, which incorporate both stability and motion.

4. Experimental Section

Banksia attenuata Samples: Cones of the highly serotinous *B. attenuata* R.Br. were collected along a climatic gradient in their natural habitats in Southwest Australia by Jessica Huss in 2014 and in 2016.[7] Prior to the experiment-specific sample preparation, single follicles were isolated from cones of the geographic locations "site 1" (29.62080 °S, 115.21177 °E), "site 2" (30.04438 °S, 115.32618 °E), and "site 5" (31.69048 °S, 115.87981 °E)[7] using a hand saw; the exocarp was removed with a chisel.

Histological Staining: Thin transverse sections of 5 µm thickness were cut with a cryo microtome (HM 560 M, Microm, Walldorf, Germany) from

© 2025 The Author(s). Advanced Functional Materials published by Wiley-VCH GmbH

a *B. attenuata* (site 2) pericarp block, containing mesocarp and endocarp. The sections were stored in water overnight, before they were stained according to the Wiesner[16c] and the improved Mäule method,[14] respectively. The stained sections were mounted on a glass slide, covered with a coverslip, and sealed with nail polish, before microscopic imaging with a digital light microscope (VHX 5000, Keyence, Osaka, Japan, objective: VH-U100UR).

Raman Microspectroscopy: Four small pericarp blocks from different *B. attenuata* follicles (site 2, block size: complete thickness over mesocarp and endocarp, 4 mm longitudinal, ≈2 mm in width) were cut in the water-saturated state with a diamond wire saw (DWS 100, Diamond WireTec, Weinheim, Germany) and clamped between small aluminum screw-jaws. The transverse surfaces of the samples were sectioned flat in the frozen state with a diamond knife (cryoimmuno 45°, DIATOME, Nidau, Switzterland) using a cryo-ultramicrotome, cooled by liquid nitrogen to −140 °C (PowerTome XL, RMC Boeckeler, Tucson, AZ, USA). Within three consecutive mesocarp fiber bundles, cross-sections of single cell walls were scanned using a Confocal Raman Microscope (alpha300, WITec, Ulm, Germany), equipped with a 60× water immersion objective (NIKON Corporation, Tokyo, Japan, NA = 1.0), using a frequency doubled linearly polarized Nd:YAG laser (λ = 532 nm, oxxius, France), and a piezo-scanner (P-500, Physik Instrumente, Karlsruhe, Germany). The measurement spots were exposed to a laser power of 22 mW, determined directly in the object area with an optical power meter. Spectra were acquired with a CCD detector cooled by a Peltier device (DU401A-BV, Andor, Belfast, North Ireland) after passing a spectrograph with a grating of 600 g mm^{-1} and a spectral resolution of 3 cm^{-1} (UHTS 300, WITec, Ulm, Germany). Two to three cell walls were scanned in each of the fiber bundles of all four samples. The measurements were conducted with the Witec Control FIVE software, and evaluated in Witec Project FIVE (version 5.2, WITec, Ulm, Germany). Cosmic ray peaks in the data were removed with a filter size of 2 and a dynamic factor of 4. The background of the spectra was subtracted by a third–order polynomial function over five manually selected mask regions in the spectra which did not contain any Raman peaks. For better comparability, the spectra were normalized to the maximum height of the 901 cm^{-1} peak, which appears to be similarly pronounced in all measurements. Peak intensity maxima were detected with the WITec Project FIVE filter function for the peaks at ≈1095, 1334, and 1598 cm^{-1}. Within the 1095 cm^{-1} peak maps of each scan, the cell wall section of high intensity—where the horizontal laser polarization matches the cellulose orientation[39]—was selected as the region of interest. From the maps of each peak (1095, 1334, and 1598 cm^{-1}), all the intensity values within the region of interest were exported and evaluated in OriginPro 2020b.

Polarizing Light Microscopy / LC-PolScope: Thin transverse sections (thickness 3 µm) were cut by means of a cryo microtome (CM1860, Leica, Wetzlar, Germany) from a *B. attenuata* (site 2) pericarp block, containing mesocarp and endocarp. They were stored in distilled water overnight before being placed on glass slides and covered with a coverslip. The sections were investigated with a liquid crystal-based polarizing light microscope (Eclipse 80i, Nikon, Tokyo, Japan, in conjunction with the LC-PolScope-System, a cooled CCD camera, and the software Abrio 1.4, CRi, Inc., Woburn, MA, USA). Images were taken in retardance mode for the qualitative evaluation of changes in the cellulose orientation within the pericarp.

Transmission Electron Microscopy: Small blocks of inner and outer mesocarp fiber bundles of *B. attenuata* (site 2) were cut wet with a diamond wire saw (DWS 100, Diamond WireTec, Weinheim, Germany). These samples were fixed with 4% paraformaldehyde and 2.5% glutaraldehyde in a 100 mM cacodylate buffer (pH 6.9) for 24 h at 4 °C. They were then stained with 3% $KMnO_4$ in acetate buffer (pH 5.6) for 2 h, and rinsed three times.[40] The samples were dehydrated in an ethanol series, before being infiltrated with Spurr's epoxy resin[41] and embedded at 70 °C for 16 h. The samples were sectioned with a diamond knife (ultra 35°, DIATOME, Nidau, Switzerland) by means of an ultramicrotome (PowerTome XL, RMC Boeckeler, Tucson, AZ, USA) at room temperature. Ultrathin longitudinal sections (thickness 100 nm) were allowed to stretch on water with chloroform vapor after cutting, and collected on Formvar-coated 200 mesh copper grids. The sections were investigated with a transmission electron microscope (JEM ARM200F, JEOL, Akishima, Japan) at 200 kV. Images were captured with a CMOS camera system and subsequently processed in Digital Micrograph (GATAN, Pleasanton, CA, USA). Overlapping detail images containing the turning point of tangential cell wall layers were stitched together and oriented within an overview image between two pits in Inkscape (version 1.0, Inkscape Project). To visualize the fine periodic pattern of cellulose and matrix, diffractograms were generated from the central detail image by the "Reduced Fast Fourier Transform" in Digital Micrograph (version 3.21.1374.0, GATAN, Pleasanton, CA, USA). Within these diffractograms the intensities of the first ring (low frequencies) were integrated azimuthally in DPDAK (version 1.4.1, DESY / MPIKG, Germany) to determine the angular dependence of the pattern with respect to the longitudinal axis of the fiber.

Hygroscopic Behavior: Thin longitudinal sections (20 µm thickness) of *B. attenuata* (site 1 and site 5) pericarp were cut with a rotary microtome (RM2255, Leica, Wetzlar, Germany). Sample areas containing the intact endocarp layer and three visually distinguishable mesocarp fiber bundles were isolated with a razor blade. The sections, nine specimens per site, were placed under a digital light microscope (VHX 5000, Keyence, Osaka, Japan, objective: VH-U100UR) on a heated microscope slide, covered with a coverslip. The samples were heated at steps of 10 K from 30 to 90 °C at 7 K min^{-1} (relative humidity in the room between 41.5% and 56.3%). Images of the samples were taken at each temperature step, 180 s after reaching the setpoint. After the 90 °C step, the samples were allowed to cool down to 30 °C again and wetted with distilled water. Images were taken after 180 s in the wet state. To evaluate the hygroscopic length changes of specific tissue directions, recognizable points were defined in the endocarp and in each mesocarp fiber bundle. Line measurements to scale were taken between these points for each temperature and moisture state with ImageJ (version 1.51n)—two measurements per tissue region and per sample. OriginPro 2015G was used for data analysis.

Tensile Stiffness: Tissue strips of endocarp and three consecutive mesocarp fiber bundles (Figure 1c) were isolated (width between 0.1 mm and 0.3 mm) with a razor blade from thin longitudinal pericarp sections (thickness: 50 µm) of *B. attenuata* (site 2). They served as specimens for the tensile tests, 10 to 14 samples per tissue region and wetting state. Two sets of samples were prepared: one set in the dry state under room conditions, and another in the wet state, immersed in 50% glycerin. The ends of the samples were glued to the edges of foliar frames with superglue (Loctite 454, Henkel AG & Co. KGaA, Düsseldorf, Germany). Each sample's test span was determined between the gluing points by imageJ line measurements on an image taken with a digital light microscope (VHX 5000, Keyence, Osaka, Japan, objective: VH-U100UR). Tensile tests were conducted using an in-house built testing stage equipped with a 2.5 N load cell (model 31E, Honeywell, Columbus, OH, USA), controlled by a LabView-based program. The expansion was captured by videoextensometry at points of high contrast near the samples' gluing points using a light microscope (SZX7, Olympus, Tokyo, Japan) equipped with a digital camera (A 102f, Basler AG, Ahrensburg, Germany).[42] One set of samples was tested in the dry state under room conditions (relative humidity between 23.1% and 24.8%, temperature between 21.6 and 23.1 °C). Another set of samples was tested in the wet state at room temperature, moistened by a continuous stream of water steam provided by a vaporizer (BH-860E, Honeywell, Charlotte, NC, USA). The samples were loaded at a tensile feed rate of 5 µm s^{-1} until material fracture (test span between 1.0 mm and 1.5 mm. Force values and the associated extension were recorded throughout the entire test. After the measurement, each sample was cut with a razor blade perpendicular to the grain. The transverse sample surfaces were imaged using an environmental scanning electron microscope (Quanta 600 FEG, FEI, Hillsboro, OR, USA). Cross-sectional areas, including inward cell lumens, were measured with imageJ (version 1.51n) for stress calculation. Data were processed using OriginPro 2015G. For each sample, the stiffness was calculated as the slope of the initial linear section of the stress-strain curve.

Nanoindentation: Blocks of *B. attenuata* (site 2) pericarp were sawn from a follicle in both the dry and the wet state and screw-tightened between small aluminum clamping jaws. The transverse surfaces of the samples were flattened with a diamond knife (cryoimmuno 45°,

© 2025 The Author(s). Advanced Functional Materials published by Wiley-VCH GmbH

DIATOME, Nidau, Switzerland) using an ultramicrotome (PowerTome XL, RMC Boeckeler, Tucson, AZ, USA). The dry nanoindentation specimen was cut at room conditions. The wet nanoindentation specimen was frozen in the water-saturated state, before sectioning under cryo conditions. Separate sample preparation for both moistening states was necessary because the pericarp tissue shows substantial deformation between the dry and the wet condition. This precludes nanoindentation measurements in both states on the same sample. A nanomechanical tester (Ubi-1, Hysitron Inc., Minneapolis, MN, USA) equipped with a Berkovich indenter was used for nanoindentation. The dry samples, three specimens, were tested under room conditions. The wet samples, two specimens, were allowed to soak distilled water through a piece of tissue from a water storage. The load-function contains three segments: Linear loading to 250 µN over the time of 2.5 s, holding at 250 µN for 15 s, linear unloading to 0 µN over the time of 2.5 s. Adjacent cells across the endocarp and within three consecutive mesocarp fiber bundles were selected for the measurements. Their cell walls were scanned with the tip of the indenter before each measurement to set the indentation points, and afterward to verify the position of the indents. Data of indents, which could be clearly associated with the fiber cell wall were, evaluated in the Hysitron testing program TriboScan and in OriginPro 2015G.

Multilayer Finite Element Model: 2D Finite element simulations were performed using Abaqus (R2019) using the Standard solver under plane strain conditions and large displacement. The geometry used had an aspect ratio of 10:3 with 20 elements in total across the thickness (5 for endocarp and 15 for the mesocarp) using E4R elements with the linear elastic material properties. Optimal mesh size was determined using a convergence analysis. A Poisson ratio of 0.3 was used for all elements, the Young's modulus was varied across the thickness by changing shrinkage and modulus values in a stepwise manner across the mesocarp thickness (10 steps in total). The gradients are all equivalent in an average sense, that is they all have same mean value (as depicted in Figure 4a). For this, we have assumed a mean value of 0.17 negative (shrinkage) strain, obtained as the average of all measured values at all locations across the mesocarp. The mean value of modulus was taken to be 2500 MPa in the mesocarp and 7500 MPa in the endocarp.

Shrinkage Stress: Single fibers of the outer mesocarp of *B. attenuata* (site 2) were isolated manually under a binocular microscope (Steindorff, Berlin) in the wet state with fine tweezers.[43] The fibers, ≈250 µm long, were allowed to dry in room conditions, before being glued with superglue (Loctite 454, Henkel AG & Co. KGaA, Düsseldorf, Germany) to the edges of sample holders, made of glass fiber reinforced polyphenylene sulfide (Tecatron GF40, Ensinger GmbH, Nufringen, Germany). After the glue hardened overnight, the response of the specimens to cyclically changing moisture regimes, inspired by the environmental humidity in their natural habitats, was tested inside a customized conditioned tensile test chamber (volume ≈160 cm^3). The chamber was cooled by a thermostat (Ministat 125 cc3, Peter Huber Kältemaschinenbau AG, Offenburg, Germany) to 20 °C through a water circuit. Humidified air for the different levels of relative humidity was provided by a humidity generator (HumiGen-04, Dr. Wernecke Feuchtemesstechnik GmbH, Potsdam, Germany) and brought into the chamber at a flow rate of 80 l h^{-1}. The climatic conditions in the chamber were constantly measured by a calibrated humidity-temperature sensor (SHT85, Sensirion AG, Stäfa, Switzerland) in vicinity to the sample. Force values were measured using a 0.5 N load cell (model 31E, Honeywell, Columbus, OH, USA), which was separately conditioned with dry air (dew point between −30 and −40 °C). A precision translation stage (M-126.DG1, Physik Instrumente GmbH & Co. KG, Karlsruhe, Germany) was used for sample position adjustment and displacement measurement. Humid air was provided by a humidity generator (Wetsys, Setaram Instrumentation, Caluire, France) at 30 °C and 77%–78% relative humidity for sample wetting. It was pumped through heated silicone tubing (temperature ≈28 °C) into a pulled and partially grounded micropipette (1 mm borosilicate capillary; World Precision Instruments, Sarasota, FL, USA; tip diameter ≈100 µm). Condensation water formed a droplet between the sample fiber and the pipette, as the tip protruded 2 mm into the 20 °C conditioned test environment. Experimental parameters were controlled by and logged in a Labview-based program (Labview, NI, Austin, TX, USA), which ran a semi-automated test procedure. It contained five fundamental humidity cycles (Figure S3, Supporting Information, Figure 5a), including four segments of force-controlled position adjustment and one drying cycle of force recording at fixed position. Hygroscopic deformation and hygroscopic stress generation of mesocarp fibers during desorption were compared, since the follicle opening steps of *B. attenuata* are related to the dry state or desorption, respectively. Images of the fiber specimens were recorded at the end of each step, at stable humidity, force, and position, using a digital microscope (VHX 5000, Keyence, Osaka, Japan, objective: VH-U100UR). Sample strain was determined based on the test span at the first wetting step (Figure S3, Supporting Information). Data was evaluated in OriginPro 2021b. Further information on the measurement procedure, the refined experimental setup, and its potential for materials research will be provided in another publication.

Supporting Information

Supporting Information is available from the Wiley Online Library or from the author.

Acknowledgements

The authors thank Klaus Bienert and Petra Leibner for their technical support during micromechanical testing, Clemens Schmitt for the discussion of the Raman data evaluation, and Ben P. Miller for the support of the project as well as linguistic and terminological advice. F.R., L.G., P.F., and M.E. acknowledge the support of the Cluster of Excellence "Matters of Activity. Image Space Material" funded by the Deutsche Forschungsgemeinschaft (DFG, German Research Foundation) under Germany's Excellence Strategy—EXC 2025–390648296. F.R., P.W., P.F., and M.E. acknowledge the funding of the Max Planck Society and the Max Planck Queensland Centre.

Conflict of Interest

The authors declare no conflict of interest.

Data Availability Statement

The data that support the findings of this study are available for download via https://doi.org/10.17617/3.9XLTTD.

Keywords

banksia, bi-layer, energy, seed release, serotiny, shape-memory, wood fibers

Received: October 2, 2024
Revised: December 16, 2024
Published online: January 23, 2025

[1] a) A. S. George, *Nuytsia* **1981**, *3*, 239; b) R. M. Cowling, B. B. Lamont, *Australian J. Ecol.* **1985**, *10*, 345.
[2] R. F. Evert, S. E. Eichhorn, *Raven Biology of plants*, W.H. Freeman and Company Publishers, New York **2013**.
[3] B. B. Lamont, D. C. Le Maitre, R. M. Cowling, N. J. Enright, *Botanical Rev.* **1991**, *57*, 277.
[4] a) R. A. Bradstock, P. J. Myerscough, *Australian J. Botany* **1981**, *29*, 521; b) N. J. Enright, B. B. Lamont, *Australian J. Ecol.* **1989**, *14*, 107; c) J. C. Huss, P. Fratzl, J. W. C. Dunlop, D. J. Merritt, B. P. Miller, M. Eder, *Front. Plant Sci.* **2019**, *10*, 283.

© 2025 The Author(s). Advanced Functional Materials published by Wiley-VCH GmbH

[5] R. M. Cowling, B. B. Lamont, *Australian J. Ecol.* **1985**, *10*, 169.
[6] A. B. Wardrop, *Australian J. Botany* **1983**, *31*, 485.
[7] J. C. Huss, V. Schoeppler, D. J. Merritt, C. Best, E. Maire, J. Adrien, O. Spaeker, N. Janssen, J. Gladisch, N. Gierlinger, B. P. Miller, P. Fratzl, M. Eder, *Adv. Sci.* **2018**, *5*, 1700572.
[8] Western Australian herbarium. Florabase – the Western Australian flora, https://florabase.dpaw.wa.gov.au/, (accessed: December 2021).
[9] J. C. Huss, O. Spaeker, N. Gierlinger, D. J. Merritt, B. P. Miller, C. Neinhuis, P. Fratzl, M. Eder, *J. R. Soc., Interface* **2018**, *15*, 20180190.
[10] a) R. Allen, A. B. Wardrop, *Australian J. Botany* **1964**, *12*, 125; b) C. Dawson, J. F. V. Vincent, A. M. Rocca, *Nature* **1997**, *390*, 668; c) W. M. Harlow, W. A. Côté, A. C. Day, *J. Forestry* **1964**, *62*, 538; d) M. J. Harrington, K. Razghandi, F. Ditsch, L. Guiducci, M. Rueggeberg, J. W. C. Dunlop, P. Fratzl, C. Neinhuis, I. Burgert, *Nat. Commun.* **2011**, *2*, 337; e) I. Shtein, R. Elbaum, B. Bar-On, *Front. Plant Sci.* **2016**, *7*, 1501; f) A. Witztum, K. Schulgasser, *J. Theor. Biol.* **1995**, *176*, 531; g) T. Lindtner, A. Y. Uzan, M. Eder, B. Bar-On, R. Elbaum, *Acta Biomater.* **2021**, *135*, 483.
[11] a) C. J. Eger, M. Horstmann, S. Poppinga, R. Sachse, R. Thierer, N. Nestle, B. Bruchmann, T. Speck, M. Bischoff, J. Rühe, *Adv. Sci.* **2022**, *9*, 2200458; b) H. Quan, A. Pirosa, W. Yang, R. O. Ritchie, M. A. Meyers, *Acta Biomater.* **2021**, *128*, 370.
[12] P. W. Rundel, M. T. K. Arroyo, R. M. Cowling, J. E. Keeley, B. B. Lamont, J. G. Pausas, P. Vargas, *Front. Plant Sci.* **2018**, *9*, 851.
[13] J. R. von Wiesner, *Sitzungsberichte der Akademie der Wissenschaften*, Mathematisch-naturwissenschaftliche Classe, Wien, **1878**.
[14] D. Yamashita, S. Kimura, M. Wada, K. Takabe, *J. Wood Sci.* **2016**, *62*, 131.
[15] C. Mäule, *Habilitation* **1901**.
[16] a) G. Meshitsuka, J. Nakano, *Mokuzai Gakkaishi* **1978**, *24*, 563; b) K. Iiyama, R. Pant, *Wood Sci. Technol.* **1988**, *22*, 167; c) F. Pomar, F. Merino, A. R. Barceló, *Protoplasma* **2002**, *220*, 17.
[17] a) C. P. Vance, T. K. Kirk, R. T. Sherwood, *Annu. Rev. Phytopathol.* **1980**, *18*, 259; b) Y. Abraham, Y. Dong, A. Aharoni, R. Elbaum, *Cellulose* **2018**, *25*, 3827.
[18] a) U. P. Agarwal, R. H. Atalla, *Planta* **1986**, *169*, 325; b) U. Agarwal, in *Advances in Lignocellulosics Characterization* (Ed: D. Argyropoulos), TAPPI Press, Atlanta **1999**; c) N. Gierlinger, *Appl. Spectrosc. Rev.* **2017**, *53*, 517.
[19] a) U. Agarwal, N. Terashima, *Proceedings* **2003**, *3*, 123; b) K. L. Larsen, S. Barsberg, *J. Phys. Chem. B* **2010**, *114*, 8009; c) L. Sun, P. Varanasi, F. Yang, D. Loqué, B. A. Simmons, S. Singh, *Biotechnol. Bioeng.* **2011**, *109*, 647.
[20] a) L. J. Gibson, *J. R. Soc., Interface* **2012**, *9*, 2749; b) H. G. M. Edwards, D. W. Farwell, D. Webster, *Spectrochim. Acta, Part A* **1997**, *53*, 2383.
[21] G. N. Christensen, K. E. Kelsey, *Holz Roh- Werkst.* **1959**, *17*, 178.
[22] Y. Abraham, R. Elbaum, *New Phytol.* **2013**, *197*, 1012.
[23] M. Eder, I. Burgert, in *Industrial Applications of Natural Fibres: Structure, Properties and Technical Applications* (Ed: J. Müssig), Wiley-VCH, Hoboken **2010**.
[24] P. Fratzl, R. Elbaum, I. Burgert, *Faraday Discuss.* **2008**, *139*, 275.
[25] a) I. Brémaud, J. Ruelle, A. Thibaut, B. Thibaut, *Holzforschung* **2013**, *67*, 75; b) M. Leonardon, C. M. Altaner, L. Vihermaa, M. C. Jarvis, *Eur. J. Wood Wood Prod.* **2010**, *68*, 87.
[26] B. A. Meylan, *Wood Sci. Technol.* **1972**, *6*, 293.
[27] a) H. A. Schroeder, *Wood Fiber Sci.* **1972**, *4*, 20; b) E. T. Engelund, L. G. Thygesen, S. Svensson, C. A. S. Hill, *Wood Sci. Technol.* **2013**, *47*, 141.
[28] a) N. Horbelt, J. W. C. Dunlop, L. Bertinetti, P. Fratzl, M. Eder, *Wood Sci. Technol.* **2021**, *55*, 1305; b) L. Salmén, *C. R. Biol.* **2004**, *327*, 873.
[29] M. Königsberger, M. Lukacevic, J. Füssl, *Mater. Struct.* **2023**, *56*, 13.
[30] P. R. Onck, E. W. Andrews, L. J. Gibson, *Int. J. Mech. Sci.* **2001**, *43*, 681.
[31] a) M. Özparpucu, M. Rüggeberg, N. Gierlinger, I. Cesarino, R. Vanholme, W. Boerjan, I. Burgert, *Plant J.* **2017**, *91*, 480; b) W. Gindl, H. S. Gupta, T. Schöberl, H. C. Lichtenegger, P. Fratzl, *Appl. Phys. A* **2004**, *79*, 2069; c) A. Jäger, T. Bader, K. Hofstetter, J. Eberhardsteiner, *Composites, Part A* **2011**, *42*, 677.
[32] M. Behl, M. Y. Razzaq, A. Lendlein, *Adv. Mater.* **2010**, *22*, 3388.
[33] P. Navi, S. Stanzl-Tschegg, *Holzforschung* **2008**, *63*, 186.
[34] a) L. Eriksson, B. Norén, *Holz Roh- Werkst.* **1965**, *23*, 201; b) P. Navi, V. Pittet, C. J. G. Plummer, *Wood Sci. Technol.* **2002**, *36*, 447.
[35] G. E. Fantner, E. Oroudjev, G. Schitter, L. S. Golde, P. Thurner, M. M. Finch, P. Turner, T. Gutsmann, D. E. Morse, H. Hansma, P. K. Hansma, *Biophys. J.* **2006**, *90*, 1411.
[36] a) M. Suchy, J. Virtanen, E. Kontturi, T. Vuorinen, *Biomacromolecules* **2010**, *11*, 515; b) E. E. Thybring, L. G. Thygesen, I. Burgert, *Cellulose* **2017**, *24*, 2375.
[37] V. Hill, *Proc. R. Soc. London, Ser. B* **1938**, *126*, 136.
[38] A. Palacios, L. Chiriatti, S. Poppinga, T. Speck, V. L. Houérou, *Adv. Intell. Syst.* **2024**, https://doi.org/10.1002/aisy.202400396.
[39] J. H. Wiley, R. H. Atalla, *Carbohydr. Res.* **1987**, *160*, 113.
[40] a) M. A. Hayat, *Fixation for Electron Microscopy*, Academic Press, New York **1981**; b) D. E. Bland, R. C. Foster, A. F. Logan, *Holzforschung* **1971**, *25*, 137.
[41] A. R. Spurr, *J. Ultrastruct. Res.* **1969**, *26*, 31.
[42] I. Burgert, K. Frühmann, J. Keckes, P. Fratzl, S. E. Stanzl-Tschegg, *Holzforschung* **2003**, *57*, 661.
[43] I. Burgert, J. Keckes, K. Frühmann, P. Fratzl, S. E. Tschegg, *Plant Biol.* **2002**, *4*, 9.
[44] a) R. Keylwerth, D. Noack, *Holz Roh- Werkst.* **1964**, *22*, 29; b) A. Patera, J. V. den Bulcke, M. N. Boone, D. Derome, J. Carmeliet, *Wood Sci. Technol.* **2017**, *52*, 91.

© 2025 The Author(s). Advanced Functional Materials published by Wiley-VCH GmbH